Dark Field Microspectroscopy with Single Molecule Fluorescence Sensitivity
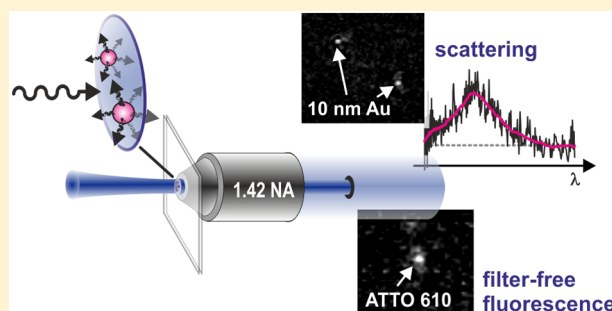
Alexander Weigel, Aleksandar Sebesta, and Philipp Kukura*

Physical and Theoretical Chemistry Laboratory, University of Oxford, South Parks Road, Oxford OX1 3QZ, United Kingdom

S *Supporting Information*

ABSTRACT: Dark field microscopy directly detects scattering from a sample by rejecting excitation light. The technique has been extensively used for spectral characterization of nanoscopic particles, but its sensitivity has been limited by residual stray light. Here, we present a simple geometry based on wide field illumination under normal incidence capable of background suppression by more than 7 orders of magnitude. The setup is optimized for spectrally resolved wide-field detection with white light illumination. We record images and spectra of single 10 nm gold particles binding to a functionalized surface, demonstrating a more than 2 orders of magnitude improvement in sensitivity over the current state of the art. Our level of stray light rejection allows us to record single molecule fluorescence images with broadband excitation without any filters in the detection path. The approach is ideally suited for investigations of truly nanoscopic objects with applications in single molecule and nanoparticle spectroscopy, plasmonic sensing, and ultrafast spectroscopy.

KEYWORDS: *dark field microscopy, scattering spectroscopy, single-molecule detection, plasmonics, background rejection*

Optical microscopy is the main tool to visualize and study microscopic or even nanoscopic structure and dynamics under nondestructive conditions. As objects decrease in size, however, it becomes increasingly challenging to differentiate the signal of interest from the underlying background, and the application of appropriate contrast mechanisms becomes essential. The ultimate background rejection can be achieved in fluorescence microscopy by suppressing excitation light with spectral filters so that single-molecule sensitivity is now routine.[1] Light-scattering based techniques have the advantage of avoiding the need for fluorescent labeling and being immune to photobleaching and blinking[2−6] but cannot take advantage of spectral filtering for background rejection. In addition, the scattering cross section rapidly drops with the particle diameter to the power of six when reducing the size of the investigated particles.[7] This dramatic decrease in scattering cross section can be reduced to a third power dependence by mixing the scattered light with a reference field[3] or by imaging refractive index changes due to photoinduced heat dissipation to the surrounding.[8] With such approaches, gold particles down to 1.4 nm diameter[8−10] and even single molecules[11−13] were recently detected. Spectral measurements on few-nanometer sized gold particles were achieved with interferometric scattering by placing a spectrometer in the detection arm,[14−16] and also indirectly by scanning the excitation wavelength in photothermal microscopy.[17] The latter approach is the counterpart to fluorescence excitation spectroscopy and characterizes the system only completely in the absence of coexisting nondissipative transitions.

Despite their success and sensitivity, all of these techniques still measure the signal of interest on top of a large background, while it is the near complete background suppression that makes fluorescence microscopy so successful. Dark field microscopy is the background-free scattering-based equivalent to fluorescence detection. Since incident and scattered light are spectrally identical, background rejection has to rely on spatial blocking of the excitation beam while detecting only those photons elastically scattered into a different direction. In combination with plasmonic labels, dark field microscopy is a powerful tool for biological imaging.[18−21] On the single particle level, the technique has been used for high speed tracking applications, for example, to resolve substeps in molecular motor motion both in vitro[22−24] and in vivo.[25,26] Dark field microscopy is particularly popular for spectrally resolved measurements because it isolates the scattered light from other contributions. It has been extensively used to study plasmon resonances in colloidal noble metal nanoparticles, including spheres,[27] rods,[28,29] disks,[4] hollow cubes,[29] shells,[30] and interfering gold disk multimers.[31] Following the spectral evolution over time allowed to directly observe metal nanoparticle growth in solution.[32] The plasmon resonance frequency of coupled gold nanoparticles is distance dependent and was proven to be a quantitative ruler for biological aggregation reactions.[33] In addition, sensitive spectral measurements have enabled the first robust label-free detection of single
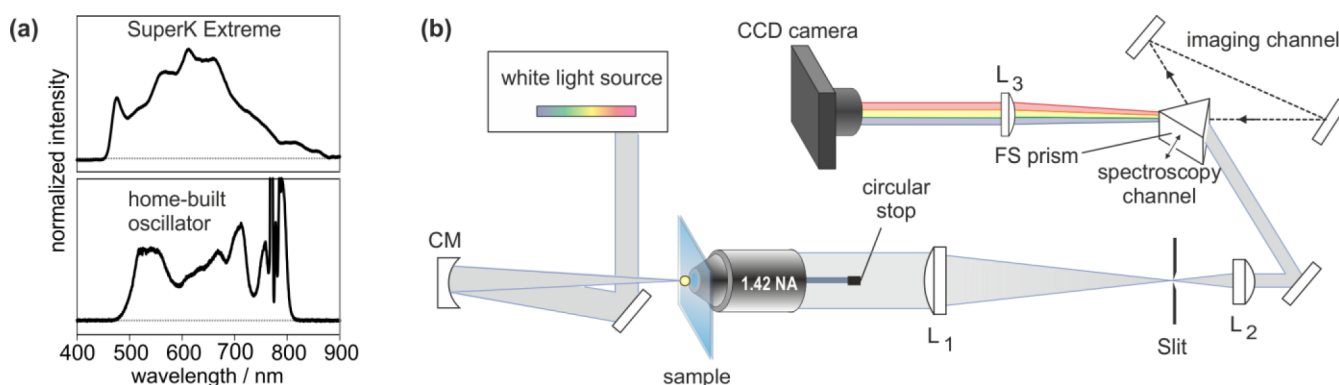
Figure 1. (a) Spectra of the two white-light laser sources used for excitation. (b) Experimental setup of the dark field microscope. CM: Curved mirror of focal length $f = 75$ mm. $L_1 - L_3$: Achromatic lenses with focal lengths of $f_1 = 200$ or 300 mm, depending on the magnification, $f_2 = 100$ mm, and $f_3 = 300$ mm. FS prism: Brewster-angle fused silica prism, which can be inserted into the beam to disperse scattered light and use the microscope in spectroscopy mode.

proteins through monitoring small shifts in the plasmon resonance of nanoscopic gold particles.[34,35]

The brightness of the signal and the background rejection efficiency determine the contrast in dark field detection. Excitation light is traditionally excluded from the detection arm by focusing an annular beam and collecting scattered light with a lower numerical aperture objective. Alternative approaches have used a small rod mirror[25,26] or a perforated mirror[22] in epi-illumination. Despite these efforts, dark field microscopy still struggles with residual stray light and the low numerical aperture in the detection arm. Since the signal intensity scales in direct detection with the sixth power of the particle size, dark field approaches have up to now been limited to signals larger than the scattering of 30 nm gold particles. High extinction of the excitation light was achieved with cross-polarization arrangements,[36,37] but the chromaticity of currently available polarizers limits these approaches to monochromatic illumination.

Here, we report background rejection of $>10^7$ with white light excitation in a simple geometry featuring wide-field illumination under normal incidence, signal collection with a high-numerical aperture objective, and excitation light rejection with a circular block. We demonstrate our sensitivity by recording dark field images and spectra of gold particles down to a size of 10 nm and by acquiring fluorescence images of single dye molecules without any filters.

■ EXPERIMENTAL SECTION

The sample was illuminated by a commercial super continuum source (SuperK Extreme, NKT Photonics) with 1−40 MHz repetition rate, or a home-built 8 MHz continuum source, details of which will be published elsewhere. The pulse spectra of both lasers are shown in Figure 1a; in some cases, the spectral range was reduced with filters, as stated in the respective results sections. Both white light sources have excellent spectral stability with intensity fluctuations on the order of 0.1−1 RMS%. The microscope setup is detailed in Figure 1b: A curved mirror ($f = 75$ mm) focuses the excitation beam under normal incidence onto the sample, which consisted either of single gold nanoparticles or dye molecules on the surface of a glass microscope slide. At a spot size of 7−10 μm (full width at half-maximum), the power density was between 0.5 and 12 kW/cm². Our illumination geometry avoids the large

intensity losses that typically accompany annular illumination and is therefore also suitable for low-power white light sources.

An oil-immersion objective with a numerical aperture of 1.42 (Olympus PLAPON) collects scattered light and fluorescence together with the transmitted excitation light. Wide field illumination under normal incidence is the key concept for effective suppression of excitation light in the detection path: The excitation beam travels straight through the center of the objective, thereby avoiding distortions and stray light generation at the periphery. Due to the large difference in numerical aperture of illumination and collection optics, the excitation beam emerges after the objective as a narrow beam of 1 mm diameter and is blocked by a 4−5.5 mm wide circular stop made of blackened aluminum. The size of the circular stop ensures effective suppression, even of the outer wings of the excitation beam, while obscuring only 20−40% of the collection beam. The resolution in this annular detection geometry remains close to the diffraction limit.[38]

After the circular stop, a telescope consisting of two achromatic lenses L_1 (depending on the magnification, $f = 200$ or 300 mm) and L_2 ($f = 100$ mm) enables spectral investigations with a slit in the focal plane. A third achromatic lens ($f = 300$ mm) focuses the detection beam onto an EMCCD camera (Qimaging Rolera Thunder), which records wide field images of the sample. Depending on magnification and binning, images were recorded with a resolution of 80−106 nm/pixel.

The microscope converts to a dark-field microspectrometer by selecting a single vertical slice of the image with a slit in the focal plane of the telescope and dispersing the light with a fused silica prism. Using the prism under Brewster conditions reduces losses and enables a total transmission in the visible of 76%. Together with the 92% quantum efficiency of the camera and the losses by the circular stop, our setup yields a total detection efficiency of 13−18% for isotropic scattering. The dispersed mode provides two-dimensional images with a spatial axis in the vertical direction and a spectrally resolved axis in the horizontal direction. The spectral detection spans 440−790 nm with 0.3 nm/pixel in the blue and 1.5 nm/pixel in the red, although these parameters are adjustable by choice of prism, camera, and magnification. We chose the slit width large enough to transmit the center part of the particle point spread function, resulting in a spectral resolution of 5 pixels. The conversion of intensity spectra into cross section spectra was calibrated with 100 nm
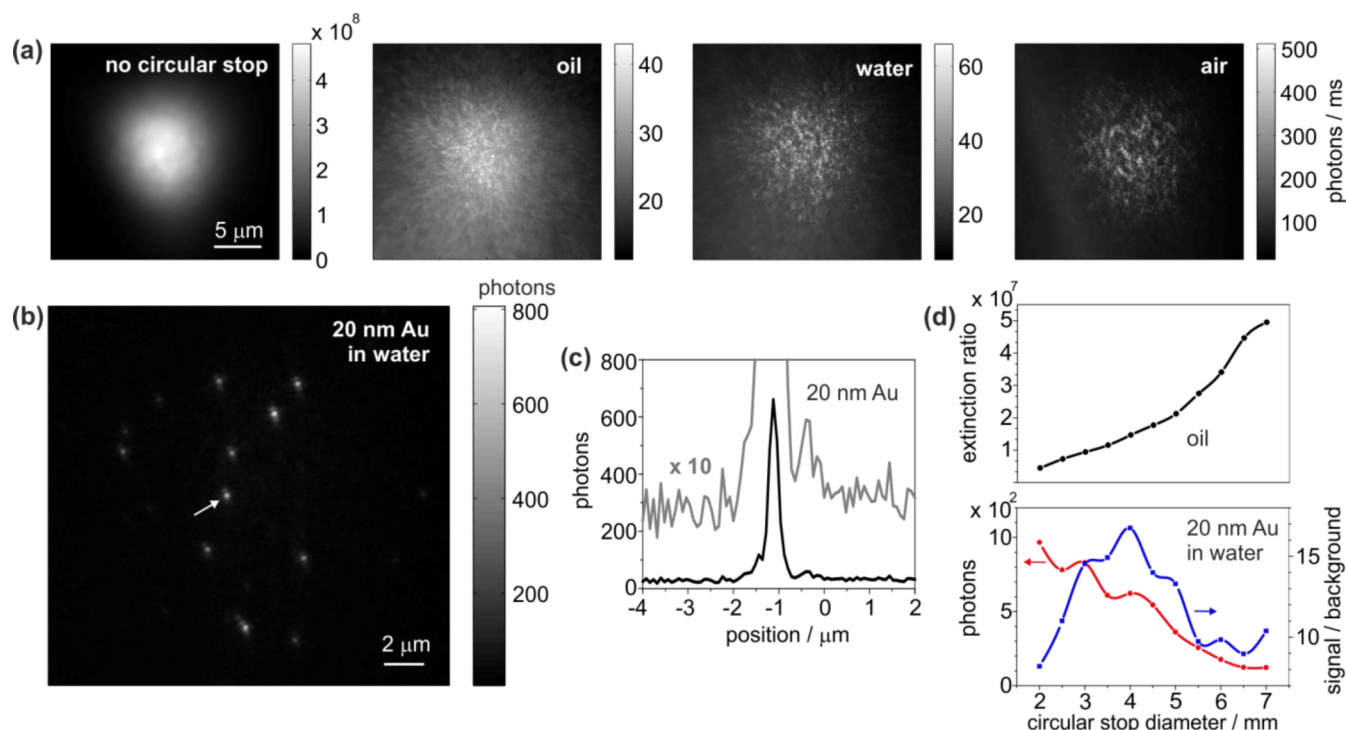
Figure 2. Characterization of front-illuminated dark field microscopy. (a) Background levels in wide field imaging mode. Excitation spot without the circular stop, and wide field image of the surface of a clean microscope glass slide covered with immersion oil, water, and air, with the excitation beam blocked by a circular stop with a 4 mm diameter. The signal level was adjusted to the dynamic range of the camera by choice of exposure time and neutral density filters and then converted back to the level of the nonattenuated beam. (b) Wide-field image of 20 nm gold particles immobilized at a glass surface and covered with Tris buffer, recorded with 1 ms integration time. (c) Line cut through the particle indicated in (b) with the arrow. (d) Effect of the circular stop diameter on the extinction ratio in oil (top) and the signal of the 20 nm gold particle marked in (c). In all cases the sample was illuminated with white light from the SuperK Extreme source with a power density of 7.4 kW/cm^2, and images were recorded with 80 nm/pixel resolution.

latex beads, which produce a smooth scattering signal that tails off with λ.[4]

■ BACKGROUND SUPPRESSION AND WIDE FIELD IMAGING CAPABILITIES

Stray light background contributes shot noise to images recorded in dark field microscopy. Hence, high sensitivity not only depends on the detection efficiency and brightness of the signal itself, but also on highly efficient background suppression. We characterized the efficiency of the circular stop for background rejection by imaging a clean glass surface covered with immersion oil under illumination with white light from the SuperK Extreme laser. The first frame in Figure 2a shows an image without the circular stop. With a 4 mm circular stop in place (second panel in Figure 2a, converted to the same photons/ms scale) the signal reduces by a factor of >10^7. In our case, remaining excitation light from multiple reflections and diffraction at the circular stop edges appears as hazy light rays in the periphery, while we attribute the structured spot in the center to sample-specific signals. It partly reproduces surface roughness of the microscope slide, which becomes visible due to the small refractive index difference between glass (n = 1.525) and immersion oil (n = 1.518). In contrast to confocal imaging, it also contains complex contributions from refractive index inhomogeneities above and below the focal plane.[39] In particular, we observe a slowly varying pattern from inhomogeneities in the viscous oil medium. The image in Figure 2 was recorded with 300 ms exposure time, so that the oil background is partly blurred. When covering the glass

surface with water or air instead of immersion oil (also shown in Figure 2a), the signal from the glass surface rises with the refractive index difference at the interface. In less viscous media, the background structure is constant over time, even for integration times as low as 1 ms.

Single gold nanoparticles are an excellent benchmark for detection sensitivity because their scattering cross sections are well understood:[2] For spherical particles, the scattering cross section decreases with the sixth power of the particle diameter, and the scattering from 30 nm gold particles is commonly regarded as the detection limit in dark field microscopy.[6] We used the same broadband illumination as for the background measurements in Figure 2a to image 20 nm gold particles at the interface between a glass microscope slide and aqueous Tris buffer solution. Figure 2b demonstrates that our setup is sensitive enough to record wide-field images of 20 nm gold particles with 1 ms integration time. The line cut in Figure 2c shows that we reach a signal/background ratio of >15 without additional corrections.

The achievable background rejection depends for given illumination conditions on the circular stop size and position. We characterized the background rejection for imaging the glass oil/interface as the average extinction ratio over a circular area with 1.5 μm diameter in the center of the excitation spot. Figure 2d, top, shows that the extinction ratio rises monotonously with circular stop size diameter. The corresponding images in the Supporting Information indicate that below a diameter of 3 mm the signal is dominated by stray light, whereas above 5.5 mm the exclusion area becomes so large that
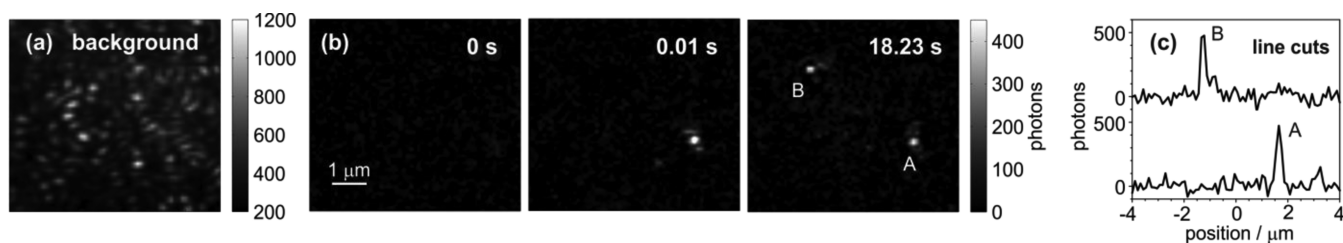
Figure 3. Streptavidin-functionalized 10 nm gold particles binding to a glass surface covered with biotinylated bovine serum albumin. (a) Background image. (b) Wide field image snap shots from a video recorded with 10 ms exposure time, with the background subtracted. (c) Line cuts through the two particles at 18.23 s. The sample was illuminated with light from 533 to 610 nm at a power density of 2.1 kW/cm^2, and images were recorded with 106 nm/pixel resolution.
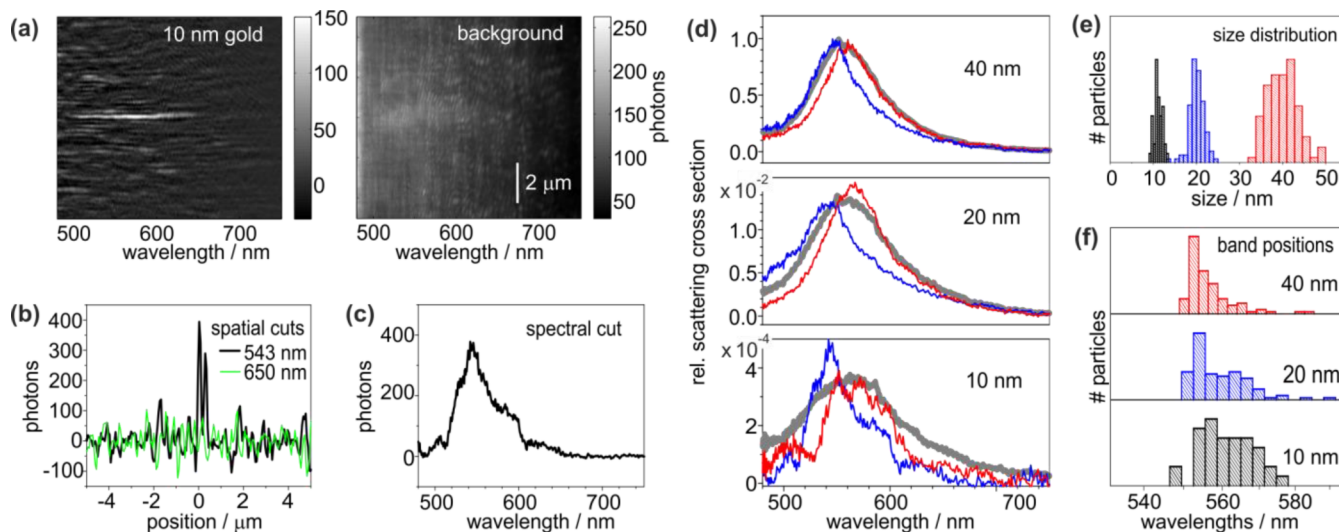

Figure 4. Dark-field spectroscopy of gold nanoparticles. (a) Dispersed image of a single 10 nm gold particle on a glass surface covered with immersion oil, and the subtracted background. The image is the average over 30 acquisitions with 500 ms exposure time, recorded at a spatial resolution of 106 nm/pixel. (b) Spatial line cuts through the image at different wavelengths. (c) Spectral line cut along the particle signal. (d) Cross section spectra from dividing the spectral cuts through the excitation spectrum, normalized to the average signal of 40 nm gold particles. Average spectra are shown in gray; blue and red are representative spectra of individual particles. (e) Particle size histograms from the sixth root of the band integral over the scattering signal, with the average 40 nm signal as the reference. (f) Histograms of the spectral centers of mass. For the histograms, 99 particles with 40 nm, 100 particles with 20 nm, and 40 particles with 10 nm nominal diameter were measured.

the entire signal decreases. For all circular stop sizes we could obtain clear images of the 20 nm gold particle sample from Figure 2b. Two effects are evident with increasing stop size: (i) The overall detected light intensity decreases as more and more light is blocked; (ii) Intensity is transferred from the center spot to the side lobes of the point spread function.[38] Both effects combined lead to a signal decrease with increasing stop diameter (red curve in Figure 2d). For the measurement reported here, we find a maximum signal/background level for 3−5 mm circular stop diameter (blue line in Figure 2d), but for optimum performance, the stop size should be adapted to the individual measurement and imaging objective used. For two-dimensional imaging, we used stop sizes of 4−4.5 mm, whereas we increased it to 5.5 mm for spectral measurements to minimize interference of stray light components with the particle signal. We found that light contamination from multiple reflections in the objective was strongly reduced by slightly misaligning the excitation and detection. As a consequence, the point spread functions are not completely symmetric, but elongate in one direction for larger stop sizes.

For 10 nm gold particles, the scattering signal reduces by another factor of 64. While we are still able to detect such signal levels, particle scattering now exhibits similar intensity levels as

the residual structured background from the glass surface. Clear images of the particles, however, can still be obtained by recording the background in the absence of the scatterers of interest. To demonstrate this, we monitored the arrival of 10 nm gold nanoparticles from aqueous Tris buffer solution at a glass surface under broadband illumination in the spectral range 533−610 nm from our home-built oscillator. Gold particles (10 nm) were injected into the pure buffer solution from one side of the flow chamber and diffused toward the detection area. We followed binding of the particles to the glass surface in continuous wide field imaging mode at a 100 Hz frame rate. By performing a median filter over a sequence of 1000 images centered at a point before the arrival of the first particle we obtained the background in Figure 3a, which resembles the structured signal from the clean glass slide in Figure 2a, but with higher photon counts. We assign the increased background to scattering from gold particles in bulk solution. Snap shots of a 6 μm × 6 μm surface area at different times are shown in Figure 3b, with time zero set arbitrarily to the frame directly before the first particle binds to the surface. Within about 18 s, two gold particles bind consecutively to the surface. Comparison of the first two frames shows that the binding event itself completes already within our acquisition time
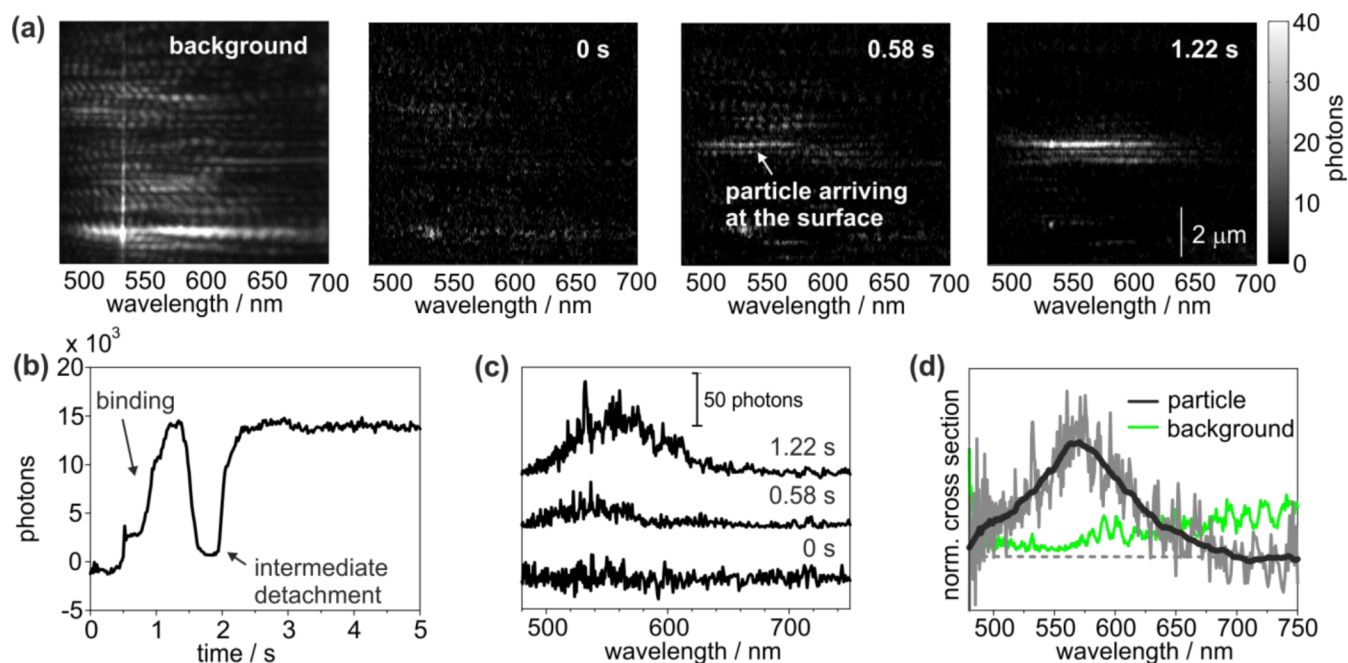
Figure 5. Spectrally resolved detection of a 10 nm gold particle binding from aqueous solution to a glass surface, recorded with 20 ms exposure time at 106 nm/pixel spatial resolution. (a) Dispersed images of the background and of the sample surface at different times. The vertical line at 532 nm originates from monochromatic laser light that was coupled in as an in situ spectral reference. (b) Time dependence of the integrated particle scattering signal. (c) Spectra of the arriving particle from line cuts through the images in (a). (d) Cross section spectrum of the gold particle at 1.22 s (gray), and the same signal after smoothing with a 50 point moving average filter (black). The spectrum of the subtracted background is also shown. The sample was illuminated with white light from the home-built oscillator at a power density of 11.2 kW/cm^2.

window of 10 ms. Residual background structure is largely due to floating particles in bulk solution (see also the Supporting Information, movie SI2). Line cuts through the particle point spread functions (Figure 2c) demonstrate a signal/noise ratio of 12 with 10 ms exposure time.

MICROSPECTROSCOPY OF SINGLE GOLD NANOPARTICLES

Our setup converts into a single particle spectrometer by closing the slit and inserting the prism into the detection arm. First we explore our absolute spectral sensitivity by imaging gold particles with minimum background at a glass−oil interface. Figure 4a shows the spectrally dispersed image of a single 10 nm gold particle after background correction. As discussed above, for 10 nm gold particles, the structured background has a similar magnitude as the scattering signal of interest. For this measurement we have used a relatively long exposure time of 500 ms to blur the scattering structure due to refractive index inhomogeneities in the oil. In less viscous aqueous solution, we did not observe a similar effect of exposure time, even at kHz frame rates. We obtained the systematic contribution to the background in Figure 4a as the median over 30 images with the particle at different positions outside the detection window, and estimated the slowly varying part of the structure, specific to our sample area, by performing a 1 μm sliding median filter along the spatial dimension of the residual. The particle signal from the corrected image has a maximum at 543 nm due to the surface plasmon resonance of the gold colloid. The residual background carries the highly structured signals from the sample interface that we did not describe in our correction procedure. The spatial line cuts in Figure 4b indicate a signal/background ratio of around 10 at the spectral maximum. The spectral line cut along the particle

signal in Figure 4c yields the scattering spectrum of the gold particle. It reproduces the typical spectral shape of a gold nanoparticle resonance, although modulated by residual background structure. Division by the spectrum of the excitation light converts it to the blue scattering cross section spectrum in Figure 4d. For comparison, we also measured spectra of particles with 40 and 20 nm diameter. Gray lines in Figure 4d are the average spectra of 40−100 particles of the corresponding size, with representative individual spectra in blue and red.

The cross section scale is given relative to the average spectral maximum of 40 nm gold particles. We characterized the total scattering cross section of each individual particle with the band integral $\int d\nu \sigma(\nu)/\nu$ of the frequency dependent cross section $\sigma(\nu)$ over the spectral range 500−650 nm, which is proportional to the transition probability,[40] and by taking the sixth root, we obtained the relative size distribution. In Figure 4e we have transferred the resulting size distribution histograms to an absolute scale by setting the average size of the 40 nm particles to exactly 40 nm. Referenced to this value, we find average sizes of 20.1 and 11.3 nm for nominally 20 and 10 nm particles, respectively.

For a consistent characterization of the plasmon resonance position for all particle sizes, we calculate the spectral centers of mass defined as $\int \nu \sigma(\nu) d\nu / \int \sigma(\nu) d\nu$. The resulting histograms are presented in Figure 4f with the corresponding wavelength axis. They have a maximum around 555 nm, in agreement with previous spectral measurements on gold particles at the glass−oil interface.[15] The plasmon resonance maximum is similar for all particle sizes, indicating that size-dependent shifts due to retardation and nonlocal effects are small in the investigated size range.[7,17,41] The distributions have a tail at the low-frequency side, which becomes more pronounced for smaller
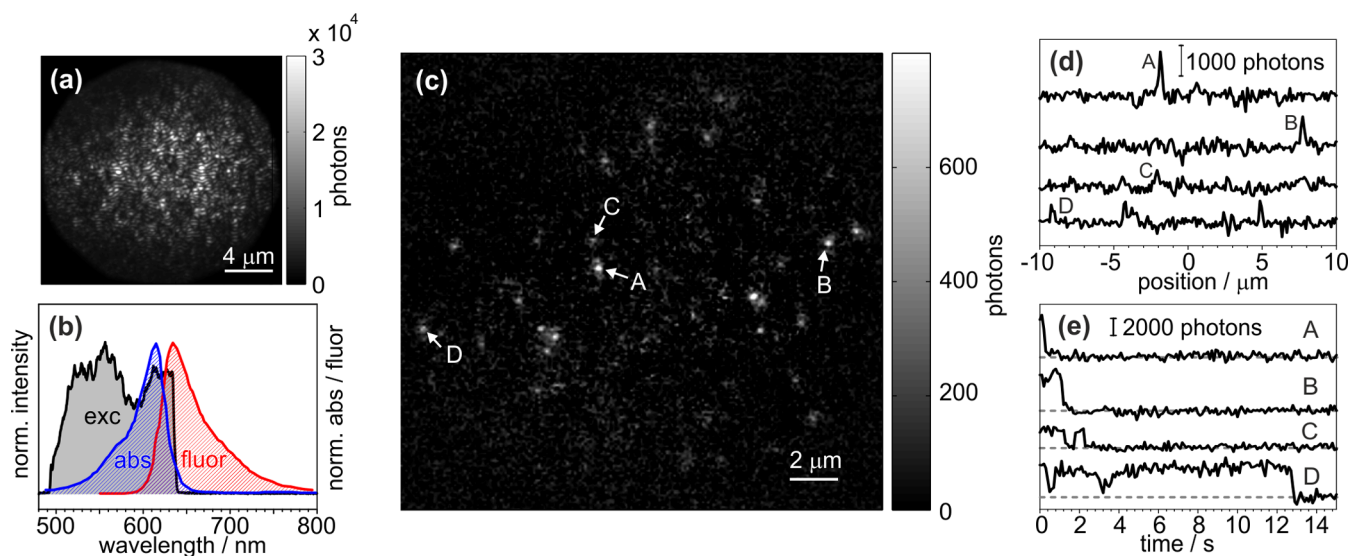
Figure 6. Filter-free dark-field imaging of single ATTO 610 molecules with 100 ms integration time. (a) Background image. The region of interest was confined with a circular aperture. (b) Spectrum of the excitation light (exc), together with the absorption (abs) and fluorescence (fluor) spectra of ATTO 610 in water. The excitation power density was 2.8 kW/cm². (c) Background-corrected fluorescence image. (d) Line cuts through the signals A−D in the fluorescence image. (e) Total emission intensities of molecules A−D over time, with the photon count indicated by the scale bar. Images were recorded with 106 nm/pixel spatial resolution.

gold particles. We explain the effect by a distortion of some particles from the ideal spherical shape, which influences smaller particles more strongly, and leads to a red-shift of the plasmon resonance.[17,42,43] The spectral shape is best defined for 20 and 40 nm particles. Residual background distorts the spectral shape of 10 nm particles, but nonetheless our sensitivity is attractive for measuring relative spectral changes, for example, in local refractive index sensing applications,[44,45] with which recently even the binding of single medium-sized proteins was detected.[34,35]

In Figure 3 we showed that the structured background can be efficiently subtracted if it is measured before the particle binds to the surface. Here we demonstrate that this approach is also applicable to dispersed detection. As before, we monitored the binding of single 10 nm particles out of Tris buffer solution to the glass surface. The sample was illuminated with the full white light spectrum from the home-built oscillator. Spectrally resolved wide field images were recorded continuously at 50 Hz frame rate. The background in Figure 5a was obtained as the average over 20 frames before the arrival of gold particles. It shows strong structure along both spatial and spectral axes. Superimposed oscillations could be due to diffraction at the circular stop edges. The line at 532 nm is the image of the slit, produced by light from a monochromatic laser, which was coupled in as a spectral reference.

Representative background-corrected images in Figure 5a document the binding of a single 10 nm gold particle. In contrast to the measurement in Figure 3, we now resolve the binding event as a gradual increase in signal intensity over the course of 1.2 s. We attribute the difference to the strong spatial confinement by the slit, which effectively leads to confocal imaging along the spectral axis and makes the experiment more sensitive to the motion of the particle in 3D. The integrated scattering signal at the particle position in Figure 5b reveals details of the binding dynamics: The initial rise of the signal is modulated by two intermediate bumps, suggesting stepwise changes during binding. At 1.5 s, the signal suddenly drops and

rises then again to the original level, indicating intermediate detachment and reattachment of the gold particle.

The spectral evolution during binding to the surface is captured by the line cuts in Figure 5c. The rise of the signal is accompanied by a spectral red-shift from initially 520 to 560 nm. A plasmon resonance maximum at 520 nm is typical for a 10 nm gold particle in water with a refractive index of $n = 1.33$. The spectral red-shift is consistent with a gradual change in local refractive index felt by the gold particle upon approaching the glass surface ($n = 1.525$) and the protein layer ($n = 1.4−1.5$). A similar change in plasmon resonance occurs again during intermediate detachment (see the Supporting Information, movie SI3). Dividing by the excitation spectrum converts the intensity spectrum at 1.22 s in Figure 5c to the cross section spectrum in Figure 5d, where the black line was obtained by applying a moving average filter. For comparison, the background spectrum is given in green. The measurement in Figure 5 was recorded with a 50 Hz frame rate, but since gold particles do not bleach, similar results should be obtainable with shorter exposure times down to the ms range by adjusting the excitation power density accordingly.[3]

■ FILTER-FREE WIDE-FIELD IMAGING OF SINGLE FLUORESCENT MOLECULES

Fluorescence microscopy has improved over the last decades to such a degree that emission from single molecules can now be detected routinely.[1] These levels of sensitivity were only possible, because background light could be almost completely suppressed with spectral filters. We now demonstrate that our excitation light rejection is high enough to image single fluorescent ATTO 610 molecules even without any filters, enabling the direct detection of resonance fluorescence. Here, we used broadband excitation light from 492 to 635 nm (gray spectrum in Figure 5b), provided by our home-built 8 MHz oscillator. Our excitation conditions are unconventional, since in single-molecule detection one usually seeks to illuminate selectively at the absorption maximum to optimize excitation efficiency. Significant absorption starts around 550 nm (blue

spectrum in Figure 6b), so that about half of our spectrum hardly interacts with the chromophore. Only the efficient stray light rejection prevents the tiny fluorescence signal from being drowned in background shot noise.

We recorded wide field images of single ATTO 610 molecules on a glass surface at 10 Hz frame rate. At the signal level of single-molecule fluorescence time-dependent changes of the background cannot be ignored any more. In our case background fluctuations mainly reflect systematic beam pointing modulations induced by air currents and mechanical drift. For background correction, we made use of the fact that after 15 s all fluorophores are photobleached. For every image we described the background as the weighted sum of several contributions, which were obtained from a singular value decomposition in a procedure outlined in the Supporting Information. Figure 6a shows a typical background image, which is dominated by the familiar structure of the glass surface (cf. Figure 2a).

The background corrected image in Figure 6c exhibits distinct fluorescence spots from single ATTO 610 emitters. Fluorescence intensities differ for individual fluorescence signals, depending on their position in the focus and the orientation of the transition dipole moment relative to the incident polarization. Line cuts through the representative emitters A−D are shown in Figure 6d. For the strongest signal, molecule A, we reach a signal/noise ratio of around 10, indicating that we approach the shot-noise limit with our background correction. The traces in panel (e) follow the integrated emission intensity of the molecules over time, demonstrating single molecule sensitivity through the observation of single step blinking and bleaching. The time interval before irreversible bleaching differs from molecule to molecule between below 1 and 13 s and is longest for fluorophores that are excited least efficiently. These experiments not only demonstrate our background rejection capabilities, but also show the capability of detecting single molecule fluorescence in spectral regions where it overlaps with the excitation light (Figure 6b). With our background correction procedure, the main noise source in this experiment is shot noise from the scattering background. Figure 2a indicates that the residual scattering from the sample surface is reduced by almost a factor of 10 when going from the glass/air to the glass/water interface. Hence, by simply covering the sample with water, fluorescence images with similar signal/noise ratios as in the current work could be recorded at 30 Hz frame rate.

CONCLUSIONS

We have presented a simple and yet effective setup for dark field imaging and spectroscopy of nanoscopic objects with the highest levels of sensitivity reported to date. The key concept is wide field illumination of the sample under normal incidence with low numerical aperture and collection of light scattering with a high numerical aperture objective. A circular stop blocks the narrow transmitted excitation beam with an extinction of >10^7, even for white light illumination. Our setup is optimized for spectrally resolved detection with 13−18% efficiency for isotropic scattering or emission, and the low losses in the excitation path allow using even weak white light sources. Gold nanoparticles served as a benchmark for our sensitivity, and we have shown images and scattering spectra of single gold particles down to a diameter of 10 nm. Structured background, visible when detecting the weakest scatterers, is sample-specific. It can be efficiently removed, as demonstrated by following the

binding of single 10 nm gold particles to a functionalized glass surface both in imaging and dispersed mode. Wide field imaging facilitates such experiments, since it allows us to monitor large sample areas with 50−100 Hz frame rate, limited here mainly by the readout speed of the CCD camera. Our setup is not only an efficient dark field microscope, but the stray light rejection is even strong enough to record fluorescence images of single molecules without any filters at 10 Hz frame rate. When going from the glass/air to the glass/water interface, it should be possible to increase the acquisition rates for filter-free fluorescence detection to 30 Hz.

One potential application of our setup is label-free sensing of single proteins through tiny spectral shifts of nanoparticle plasmon resonances induced by local refractive index changes.[34,35] The observed shifts are strongest for smaller particle sizes,[46] and the localization precision for the spectral position depends on the signal contrast. Our sensitivity could allow detection of even small proteins or resolve binding events in more detail. The wide field imaging capabilities are ideal for the simultaneous readout of multiple plasmonic sensors. We note that our excitation geometry is also ideal for experiments with femtosecond pulses: Ultrafast microscopy is commonly hampered by the severe phase distortions the objective imposes onto the pulses. We avoid any temporal dispersion in the excitation beam by focusing with a low numerical aperture concave mirror onto the sample. Together with the ability to record single molecule fluorescence images even under resonance with the illumination beam, tailored broadband pump-depletion experiments could be designed to control the electronic population flow in the ground and excited states.

METHODS

Microscope slides were bath-sonicated in a 1:1 isopropanol/ water mixture and subsequently plasma-treated. For experiments in which the surface was covered with a liquid, we constructed a flow chamber with a second cover glass or an antireflective coated BK7 window, and several layers of double-sided tape as a spacer.

For experiments at the glass/water interface streptavidin-functionalized gold particles were bound via a streptavidin−biotin linker to the microscope slide. The glass surface was incubated for 5 min with a solution of 1 mg/mL biotinylated-bovine serum albumin (biotin-BSA, Sigma) in TRIS buffer with 50 mM sodium chloride (Sigma, pH 7.8), diluted 100-fold with nonmodified BSA solution (Sigma) of the same concentration. The functionalized surface was then covered with pure TRIS buffer, and an aqueous solution of streptavidin-functionalized gold particles (EM.STP line, Life Technology) was added, leading to an equilibrium bulk concentration of 50 pM. Samples of gold particles at the glass/oil interface were prepared by spin-coating aqueous solutions of bare nanoparticles (EM.GC line, BBI Solutions) onto the microscope slide and then covering the surface with immersion oil (OLYMPUS, Type F). For single molecule experiments, the manufacturer-supplied ATTO 610 solution (ATTO-TEC) was 10^6-fold diluted with Milli-Q water and spin-coated onto a microscope slide.

ASSOCIATED CONTENT

Ⓢ Supporting Information

Individual measurements of circular stop size dependence and gold particle spectra, and a description of the background correction procedure based on singular-value decomposition are presented. In addition, movies accompanying Figures 3, 5,

and 6 are provided. This material is available free of charge via the Internet at http://pubs.acs.org.

■ AUTHOR INFORMATION

Corresponding Author
*E-mail: philipp.kukura@chem.ox.ac.uk.

Notes
The authors declare no competing financial interest.

■ REFERENCES

(1) Moerner, W. E.; Orrit, M. Illuminating single molecules in condensed matter. *Science* **1999**, *283*, 1670−1676.

(2) van Dijk, M. A.; Tchebotareva, A. L.; Orrit, M.; Lippitz, M.; Berciaud, S.; Lasne, D.; Cognet, L.; Lounis, B. Absorption and scattering microscopy of single metal nanoparticles. *Phys. Chem. Chem. Phys.* **2006**, *8*, 3486−3495.

(3) Ortega-Arroyo, J.; Kukura, P. Interferometric scattering microscopy (iSCAT): new frontiers in ultrafast and ultrasensitive optical microscopy. *Phys. Chem. Chem. Phys.* **2012**, *14*, 15625−15636.

(4) Sönnichsen, C.; Geier, S.; Hecker, N. E.; von Plessen, G.; Feldmann, J.; Ditlbacher, H.; Lamprecht, B.; Krenn, J. R.; Aussenegg, F. R.; Chan, V. Z.-H.; Spatz, J. P.; Möller, M. Spectroscopy of single metallic nanoparticles using total internal reflection microscopy. *Appl. Phys. Lett.* **2000**, *77*, 2949−2951.

(5) Kukura, P.; Ewers, H.; Müller, C.; Renn, A.; Helenius, A.; Sandoghdar, V. High-speed nanoscopic tracking of the position and orientation of a single virus. *Nat. Methods* **2009**, *6*, 923−927.

(6) Zijlstra, P.; Orrit, M. Single metal nanoparticles: optical detection, spectroscopy and applications. *Rep. Prog. Phys.* **2011**, *74*, 106401.

(7) Pelton, M.; Bryant, G. *Introduction to Metal-Nanoparticle Plasmonics*; John Wiley & Sons, Inc.: New York, 2013.

(8) Boyer, D.; Tamarat, P.; Maali, A.; Lounis, B.; Orrit, M. Photothermal imaging of nanometer-sized metal particles among scatterers. *Science* **2002**, *297*, 1160−1163.

(9) Berciaud, S.; Cognet, L.; Blab, G. A.; Lounis, B. Photothermal heterodyne imaging of individual nonfluorescent nanoclusters and nanocrystals. *Phys. Rev. Lett.* **2004**, *93*, 257402.

(10) Jacobsen, V.; Stoller, P.; Brunner, C.; Vogel, V.; Sandoghdar, V. Interferometric optical detection and tracking of very small gold nanoparticles at a water-glass interface. *Opt. Express* **2006**, *14*, 405−414.

(11) Kukura, P.; Celebrano, M.; Renn, A.; Sandoghdar, V. Single-molecule sensitivity in optical absorption at room temperature. *J. Phys. Chem. Lett.* **2010**, *1*, 3323−3327.

(12) Gaiduk, A.; Yorulmaz, M.; Ruijgrok, P. V.; Orrit, M. Room-temperature detection of a single molecule's absorption by photo-thermal contrast. *Science* **2010**, *330*, 353−356.

(13) Chong, S.; Min, W.; Sunney Xie, X. Ground-state depletion microscopy: detection sensitivity of single-molecule optical absorption at room temperature. *J. Phys. Chem. Lett.* **2010**, *1*, 3316−3322.

(14) Stoller, P.; Jacobsen, V.; Sandoghdar, V. Measurement of the complex dielectric constant of a single gold nanoparticle. *Opt. Lett.* **2006**, *31*, 2474−2476.

(15) Lindfors, K.; Kalkbrenner, T.; Stoller, P.; Sandoghdar, V. Detection and spectroscopy of gold nanoparticles using super-continuum white light confocal microscopy. *Phys. Rev. Lett.* **2004**, *93*, 037401.

(16) Palomba, S.; Novotny, L.; Palmer, R. E. Blue-shifted plasmon resonance of individual size-selected gold nanoparticles. *Opt. Commun.* **2008**, *281*, 480−483.

(17) Berciaud, S.; Cognet, L.; Tamarat, P.; Lounis, B. Observation of intrinsic size effects in the optical response of individual gold nanoparticles. *Nano Lett.* **2005**, *5*, 515−518.

(18) Wax, A.; Sokolov, K. Molecular imaging and darkfield microspectroscopy of live cells using gold plasmonic nanoparticles. *Laser Photon. Rev.* **2009**, *3*, 146−158.

(19) Li, Y.; Jing, C.; Zhang, L.; Long, Y.-T. Resonance scattering particles as biological nanosensors in vitro and in vivo. *Chem. Soc. Rev.* **2012**, *41*, 632−642.

(20) Ringe, E.; Sharma, B.; Henry, A.-I.; Marks, L. D.; Van Duyne, R. P. Single nanoparticle plasmonics. *Phys. Chem. Chem. Phys.* **2013**, *15*, 4110−4129.

(21) Dreaden, E. C.; Alkilany, A. M.; Huang, X.; Murphy, C. J.; El-Sayed, M. A. The golden age: gold nanoparticles for biomedicine. *Chem. Soc. Rev.* **2012**, *41*, 2740−2779.

(22) Ueno, H.; Nishikawa, S.; Iino, R.; Tabata, K. V.; Sakakihara, S.; Yanagida, T.; Noji, H. Simple dark-field microscopy with nanometer spatial precision and microsecond temporal resolution. *Biophys. J.* **2010**, *98*, 2014−2023.

(23) Yasuda, R.; Noji, H.; Yoshida, M.; Kinosita, K.; Itoh, H. Resolution of distinct rotational substeps by submillisecond kinetic analysis of F₁-ATPase. *Nature* **2001**, *410*, 898−904.

(24) Nishiyama, M.; Muto, E.; Inoue, Y.; Yanagida, T.; Higuchi, H. Substeps within the 8 nm step of the ATPase cycle of single kinesin molecules. *Nat. Cell Biol.* **2001**, *3*, 425−428.

(25) Sowa, Y.; Steel, B. C.; Berry, R. M. A simple backscattering microscope for fast tracking of biological molecules. *Rev. Sci. Instrum.* **2010**, *81*, 113704.

(26) Nan, X.; Sims, P. A.; Sunney Xie, X. Organelle tracking in a living cell with microsecond time resolution and nanometer spatial precision. *ChemPhysChem* **2008**, *9*, 707−712.

(27) Tcherniak, A.; Ha, J. W.; Dominguez-Medina, S.; Slaughter, L. S.; Link, S. Probing a century old prediction one plasmonic particle at a time. *Nano Lett.* **2010**, *10*, 1398−1404.

(28) Sönnichsen, C.; Franzl, T.; Wilk, T.; von Plessen, G.; Feldmann, J.; Wilson, O.; Mulvaney, P. Drastic reduction of plasmon damping in gold nanorods. *Phys. Rev. Lett.* **2002**, *88*, 077402.

(29) Hu, M.; Novo, C.; Funston, A.; Wang, H.; Staleva, H.; Zou, S.; Mulvaney, P.; Xia, Y.; Hartland, G. V. Dark-field microscopy studies of single metal nanoparticles: understanding the factors that influence the linewidth of the localized surface plasmon resonance. *J. Mater. Chem.* **2008**, *18*, 1949−1960.

(30) Nehl, C. L.; Grady, N. K.; Goodrich, G. P.; Tam, F.; Halas, N. J.; Hafner, J. H. Scattering spectra of single gold nanoshells. *Nano Lett.* **2004**, *4*, 2355−2359.

(31) Fan, J. A.; Bao, K.; Lassiter, J. B.; Bao, J.; Halas, N. J.; Nordlander, P.; Capasso, F. Near-normal incidence dark-field microscopy: applications to nanoplasmonic spectroscopy. *Nano Lett.* **2012**, *12*, 2817−2821.

(32) Herrmann, L. O.; Baumberg, J. J. Watching single nanoparticles grow in real time through supercontinuum spectroscopy. *Small* **2013**, *9*, 3743−3747.

(33) Sönnichsen, C.; Reinhard, B. M.; Liphardt, J.; Alivisatos, A. A molecular ruler based on plasmon coupling of single gold and silver nanoparticles. *Nat. Biotechnol.* **2005**, *23*, 741−745.

(34) Zijlstra, P.; Paulo, P. M. R.; Orrit, M. Optical detection of single non-absorbing molecules using the surface plasmon resonance of a gold nanorod. *Nat. Nanotechnol.* **2012**, *7*, 379−382.

(35) Ament, I.; Prasad, J.; Henkel, A.; Schmachtel, S.; Sönnichsen, C. Single unlabeled protein detection on individual plasmonic nano-particles. *Nano Lett.* **2012**, *12*, 1092−1095.

(36) Hong, X.; van Dijk, E. M. P. H.; Hall, S. R.; Götte, J. B.; van Hulst, N. F.; Gersen, H. Background-free detection of single 5 nm

nanoparticles through interferometric cross-polarization microscopy. *Nano Lett.* **2011**, *11*, 541−547.

(37) Kuhlmann, A. V.; Houel, J.; Brunner, D.; Ludwig, A.; Reuter, D.; A. D. Wieck, R. W. A dark-field microscope for background-free detection of resonance fluorescence from single semiconductor quantum dots operating in a set-and-forget mode. *Rev. Sci. Instrum.* **2013**, *84*, 073905.

(38) McGloin, D.; Dholakia, K. Bessel beams: diffraction in a new light. *Contemp. Phys.* **2005**, *46*, 15−28.

(39) Shaw, P. J. Comparison of widefield/deconvolution and confocal microscopy for three-dimensional imaging. In *Handbook of Biological Confocal Microscopy*, 3rd edition; Pawley, J. B., Ed.; Springer Science + Business Media: New York, 2006; pp 453−467.

(40) Mataga, N.; Kubota, T. *Molecular Interactions and Electronic Spectra*; Marcel Dekker, Inc.: New York, 1970.

(41) Link, S.; El Sayed, M. A. Shape and size dependence of radiative, non-radiative and photothermal properties of gold nanocrystals. *Int. Rev. Phys. Chem.* **2000**, *19*, 409−453.

(42) Orendorff, C. J.; Sau, T. K.; Murphy, C. J. Shape-dependent plasmon-resonant gold nanoparticles. *Small* **2006**, *2*, 636−639.

(43) Mock, J. J.; Barbic, M.; Smith, D. R.; Schultz, D. A.; Schultz, S. Shape effects in plasmon resonance of individual colloidal silver nanoparticles. *J. Chem. Phys.* **2002**, *116*, 6755−6759.

(44) McFarland, A. D.; Van Duyne, R. P. Single silver nanoparticles as real-time optical sensors with zeptomole sensitivity. *Nano Lett.* **2003**, *3*, 1057−1062.

(45) Raschke, G.; Kowarik, S.; Franzl, T.; Sönnichsen, C.; Klar, T. A.; Feldmann, J.; Nichtl, A.; Kürzinger, K. Biomolecular recognition based on single gold nanoparticle light scattering. *Nano Lett.* **2003**, *3*, 935−938.

(46) Shen, H.; Lu, G.; Zhang, T.; Liu, J.; Gu, Y.; Perriat, P.; Martini, M.; Tillement, O.; Gong, Q. Shape effect on a single-nanoparticle-based plasmonic nanosensor. *Nanotechnology* **2013**, *24*, 285502.